Center for Turbulence Research
Proceedings of the Summer Program 2006

Numerical simulation of flow- and combustion-induced sound using a hybrid LES/CAA approach

By M. Ihme, M. Kaltenbacher† AND H. Pitsch

A hybrid LES/CAA approach for the numerical prediction of combustion-induced noise applicable to complex geometries is developed. This hybrid method is based on a low Mach number variable density LES solver combined with a finite element (FE) code for the computation of the acoustic field. The acoustic field is modeled using two different analogies, namely Lighthill's acoustic analogy and Phillips' equation. Whereas Lighthill's analogy considers the sound propagation into a homogeneous medium, Phillips' equation accounts for acoustic refraction effects due to variations of the sound speed. The hybrid LES/CAA approach is applied in numerical simulations of an N_2-diluted CH_4-H_2/air flame. The source-terms, appearing in both models, are analyzed and the effect of the variable sound speed on the directivity is investigated. Numerical results obtained from both models are compared with experimental data. Reasonable agreement of the sound pressure level is obtained in the low-frequency range; the over-prediction of the sound pressure level at higher frequencies requires further investigation.

1. Motivation

Noise generated from technical devices is an increasingly important problem. Jet engines in particular produce sound levels that are not only a nuisance, but may also impair hearing. The noise emitted by such engines is generated by different sources such as jet exhaust, fans or turbines, and combustion. Increasing restrictions on the allowable noise-emission levels force manufacturers to design quieter engines. This, however, represents a challenging task because the underlying physical phenomena of the aerodynamic sound generation are yet not entirely understood. Furthermore, design changes made to comply with noise-emission regulations may be accompanied by losses in performance. Numerical simulations offer promise as a tool to address this design challenge, if adequate models are available. Specifically, the Large-Eddy Simulation (LES) technique was demonstrated to be able to predict complex turbulent flow configurations.

This work addresses the topic of combustion-generated noise at low Mach numbers. A method for the prediction of the acoustic far field pressure emitted by an open non-premixed turbulent flame has been proposed by Ihme *et al.* (2006). This model is based on Lighthill's acoustic analogy (Lighthill 1952) and employs a flamelet/progress variable model (Pierce & Moin 2004) in modeling the acoustic source-terms. The application of this method is restricted to unconfined flows. Furthermore, flow/acoustic interactions, which mainly arise due to strong changes of the sound speed in the acoustic source region, cannot be accounted for with this theory. A hybrid methodology is developed in

† Department of Sensor Technology, Friedrich Alexander University Erlangen, Germany

which a low Mach number variable-density LES solver is combined with a finite element (FE) code to predict noise generated by combustion. The advantage of this method is that it can be applied to complex flow configurations and facilitates an environment for the numerical simulation of practical noise problems. Kotake (1975) and Poinsot & Veynante (2001) derived an acoustic analogy from the conservation equation for mass, momentum, and temperature. Because of its strong resemblance to the acoustic analogy proposed by Phillips (1960), we will refer to this analogy as Phillips' equation. Even though the wave operator in this equation does not contain all terms appearing in a moving-media wave equation, this analogy accounts for interaction of the mean flow with the sound (Doak 1972). This is different from Lighthill's analogy, since that propagation operator does not account for refraction effects due to the sound speed.

The objective of this paper is the assessment of both Lighthill's and Phillips' analogy as predictive models for sound generated by turbulent combustion. A key point is the validation of the numerical results with experimental data. The lack of the availability of a comprehensive experimental data set for flow-field quantities and acoustic data for confined geometries limits our application to an open, non-premixed turbulent flame, which has been experimentally studied by Bergmann *et al.* (1998), Meier *et al.* (2000), Schneider *et al.* (2003), and Singh *et al.* (2003, 2004). Special interest is devoted to the analysis of the spatial distribution and temporal behavior of the different source-terms in both analogies. A considerable amount of previous work has been devoted to the study of sound refraction effects due to mean shear in isothermal jets (Pao 1973; Balsa 1976; Durbin 1983*a*,*b*). To the authors' knowledge, the influence of the strong temperature changes in reactive jet flames on the acoustic refraction has not been studied. The effect of the variation of the sound speed in the source region on the directivity pattern is analyzed using Phillips' equation.

The remainder of the paper is organized in the following manner. The mathematical model for the hybrid LES/CAA method is presented in Section 2. The experimental configuration, computational setup for the LES, and the acoustic simulation is described in Section 3. Results obtained with the different models are compared in Section 4, followed by conclusions.

2. Mathematical model

2.1. *Governing equations and combustion model*

The instantaneous equations describing conservation of mass, momentum, mixture fraction, progress variable, and temperature can be written in non-dimensional form as

$$\mathcal{D}_\tau \rho = -\rho \nabla_{\boldsymbol{y}} \cdot \boldsymbol{u}\,, \tag{2.1a}$$

$$\rho \mathcal{D}_\tau \boldsymbol{u} = -\nabla_{\boldsymbol{y}} p + \frac{1}{\mathrm{Re}} \nabla_{\boldsymbol{y}} \cdot \underline{\underline{\sigma}}\,, \tag{2.1b}$$

$$\rho \mathcal{D}_\tau z = \frac{1}{\mathrm{Re}\,\mathrm{Sc}} \nabla_{\boldsymbol{y}} \cdot (\rho\alpha \nabla_{\boldsymbol{y}} z)\,, \tag{2.1c}$$

$$\rho \mathcal{D}_\tau c = \frac{1}{\mathrm{Re}\,\mathrm{Sc}} \nabla_{\boldsymbol{y}} \cdot (\rho\alpha \nabla_{\boldsymbol{y}} c) + \mathrm{Da}\,\rho\dot{\omega}_c\,, \tag{2.1d}$$

$$\begin{aligned} \rho c_\mathrm{p} \mathcal{D}_\tau \theta = {} & \frac{1}{\mathrm{Re}\,\mathrm{Sc}} \nabla_{\boldsymbol{y}} \cdot (\lambda \nabla_{\boldsymbol{y}} \theta) + \mathrm{Da}\rho\dot{\omega}_\theta + \mathrm{Ec}\,\mathcal{D}_\tau p \\ & + \frac{1}{\mathrm{Re}\,\mathrm{Sc}} \left(\rho\alpha \sum_k c_{\mathrm{p},k} \nabla_{\boldsymbol{y}} y_k \right) \cdot \nabla_{\boldsymbol{y}} \theta + \frac{\mathrm{Ec}}{\mathrm{Re}} \underline{\underline{\sigma}} : \nabla_{\boldsymbol{y}} \boldsymbol{u}\,, \end{aligned} \tag{2.1e}$$

in which $\rho, \boldsymbol{u}, p, \underline{\underline{\sigma}}, z, c$ are the density, the velocity vector, the pressure, the viscous stress tensor, the mixture fraction, and the progress variable, respectively. The dimensionless temperature is denoted by θ, c_p is the specific heat at constant pressure, λ is the heat diffusion coefficient, and $\dot{\omega}_\psi$ is the source-term corresponding to the scalar ψ. The substantial derivative is denoted by $\mathcal{D}_\tau = \partial_\tau + \boldsymbol{u} \cdot \nabla_{\boldsymbol{y}}$. Here the time-space coordinate $(\tau, \boldsymbol{y})$ refers to the source region. In the following, a cylindrical coordinate system with $\boldsymbol{y} = (r, \varphi, y)$ is employed. The above equations are written under the assumption of unity Lewis number in which case the diffusion velocity can be expressed by Fick's law. From the non-dimensionalization, the following dimensionless groups arise in Eqs. (2.1): The Reynolds number is denoted by Re, the Schmidt number is Sc, the Damköhler number is Da, and the Eckert number is Ec. Note that inner parameters, i.e., characteristic scales associated with the turbulent reactive flow field, are used as reference quantities. The set of dimensionless variables used to obtain Eqs. (2.1) are given in Ihme *et al.* (2006).

The jet exit Mach number $\mathrm{M_J}$, defined by the exit velocity U_ref and the reference speed of sound a_ref,

$$\mathrm{M_J} = \frac{U_\mathrm{ref}}{a_\mathrm{ref}} \,, \tag{2.2}$$

is approximately $\mathrm{M_J} \approx \mathcal{O}(0.1)$ for the experimental configuration considered below. The flow velocity in a jet decreases inversely with the streamwise nozzle distance. Furthermore, the temperature, and hence the sound speed, increase with axial distance by heat release due to exothermic chemical reactions. Both effects then lead to a further reduction of the local Mach number $\mathrm{M} = u_x(\boldsymbol{x})/a(\boldsymbol{x})$ so that $\mathrm{M} \leq \mathrm{M_J}$. This low-speed jet flame application motivates the usage of a low-Mach number variable density LES code for the simulation of the turbulent reactive flow field and the acoustic source-term distribution.

The system of equations given in (2.1) is solved here in the following way. Equations (2.1*a*) and (2.1*b*) have five unknowns, ρ, $\boldsymbol{u}$, and p. Here, the low Mach number limit is considered, and the continuity equation is replaced by a Poisson equation for the pressure. The computation of the density then requires an equation of state, which is given in the form

$$\rho = \rho(z, c) \,. \tag{2.3}$$

Equation (2.3) constitutes the so-called flamelet/progress variable (FPV) model (Pierce & Moin 2004), in which all chemical and thermodynamic quantities, denoted by $\boldsymbol{\psi}$, are expressed in terms of the mixture fraction and the progress variable. This model requires the solution of transport equations for z and c which are given by Eqs. (2.1*c*) and (2.1*d*). The functional relation $\boldsymbol{\psi} = \boldsymbol{\psi}(z, c)$ is obtained from a steady flamelet model.

Note that the temperature equation (2.1*e*) is not directly solved for. It is presented here for completeness and is used to derive Phillips' wave equation in Section 2.2.2.

2.2. *Acoustic model and FE formulation*

In this section the two acoustic analogies are presented, major model assumptions, and differences between both analogies are discussed. Both model equations are solved using an FE formulation and will be discussed in Section 2.2.3.

2.2.1. *Lighthill's acoustic analogy*

In Lighthill's acoustic analogy (Lighthill 1952), the turbulent eddies and, in the case of reactive flows, the unsteady heat release are regarded as convected acoustic sources. The acoustic sources and pressure fluctuations are considered to propagate in a homogeneous stagnant medium, having constant properties. Lighthill derived a wave equation from

the conservation equation of mass and momentum by performing the operation $\partial_\tau(2.1a)$-$\nabla_{\boldsymbol{y}}\cdot(2.1b)$ and adding the term $a_{\rm ref}^{-2}\partial_\tau^2 p$ to both sides, resulting in

$$a_{\rm ref}^{-2}\partial_\tau^2 p - \Delta_{\boldsymbol{y}} p = \nabla_{\boldsymbol{y}}\cdot\nabla_{\boldsymbol{y}}\cdot\left(\rho\boldsymbol{u}\boldsymbol{u} - \frac{1}{\mathrm{Re}}\underline{\underline{\sigma}}\right) - \partial_\tau^2(\rho - a_{\rm ref}^{-2}p)\,. \tag{2.4}$$

The argument of the last term on the right-hand side (RHS) of Eq. (2.4) is termed "excess density", and is denoted by $\rho_{\rm e}$. Using Eq. (2.3), the variation of $\rho_{\rm e}$ can be expressed in terms of z and c. With this, the acoustic sources due to entropy variation in the source region can be written as (Ihme *et al.* 2006)

$$\partial_\tau^2\rho_{\rm e} = \mathrm{Da}\partial_\tau\left(\frac{\dot\omega_c}{\rho}\partial_C\rho\right) + \partial_\tau\nabla_{\boldsymbol{y}}\cdot((1-\rho)\boldsymbol{u}) - a_{\rm ref}^{-2}\partial_\tau(p-p_{\rm ref}) + \mathcal{O}(\mathrm{Ec},\mathrm{Re}^{-1})\,. \tag{2.5}$$

Note that in the following, source-term contributions which are of the order $\mathcal{O}(\mathrm{Ec},\mathrm{Re}^{-1})$ and the pressure fluctuation on the RHS of the wave equation are neglected. This is mainly motivated by dimensional arguments. The validity of this assumption for reactive turbulent flows requires further investigation. With this, the model-wave equation following Lighthill's analogy reads as

$$a_{\rm ref}^{-2}\partial_\tau^2 p' - \Delta_{\boldsymbol{y}} p' = \nabla_{\boldsymbol{y}}\cdot\nabla_{\boldsymbol{y}}\cdot(\rho\boldsymbol{u}\boldsymbol{u}) \underbrace{-\partial_\tau\nabla_{\boldsymbol{y}}\cdot((1-\rho)\boldsymbol{u}) - \mathrm{Da}\partial_\tau\left(\dot\omega_c\partial_C\ln(\rho)\right)}_{-\partial_\tau^2\rho}\,. \tag{2.6}$$

The first term on the RHS is a source-term due to unsteady Reynolds stresses and also indirectly contains refractive effects, the second term is a fluctuating momentum flux, and the third term represents an acoustic source-term due to the unsteady reaction rate.

Lighthill's wave equation is formulated so that a linear propagation operator for the pressure fluctuation is on the LHS and all non-linear terms are lumped together on the RHS. The interaction of the sound with the mean flow and the variation in the refraction index due to changes in the local speed of sound result in refraction of the sound, in a change of the directivity, and in a "zone of relative silence" in the jet-forward angle at high frequencies (Balsa 1976; Pao 1973; Ffowcs Williams 1977). These flow/acoustic interactions, which are only indirectly accounted for by the RHS of Lighthill's analogy, are of importance for the accurate jet-noise prediction (Lush 1971). A model equation accounting for effects due to variable sound speed is presented in the next section.

2.2.2. *Phillips' equation for variable speed of sound*

A wave equation accounting for effects of convection and refraction of sound waves by mean flow and inhomogeneities in the media can be derived from conservation equations of mass, momentum, temperature, and the ideal gas law (Kotake 1975; Poinsot & Veynante 2001)

$$p = \frac{1}{\mathrm{Ec}}\rho R\theta = \frac{1}{\gamma}a^2\rho\,, \tag{2.7}$$

written in non-dimensional form. The gas constant and the variable sound speed are denoted by R and a, respectively. After neglecting terms of order $\mathcal{O}(\mathrm{Ec},\mathrm{Re}^{-1})$ Eqs. (2.1b) and (2.1e) can be written as

$$\frac{a^2}{\gamma}\nabla_{\boldsymbol{y}}\ln(p) = -\mathcal{D}_\tau\boldsymbol{u}\,, \tag{2.8a}$$

$$\frac{1}{\gamma}\mathcal{D}_\tau\ln(p) = -\nabla_{\boldsymbol{y}}\cdot\boldsymbol{u} + \mathcal{D}_\tau\ln(R) + \frac{\mathrm{Da}}{c_{\rm p}\theta}\dot\omega_\theta\,. \tag{2.8b}$$

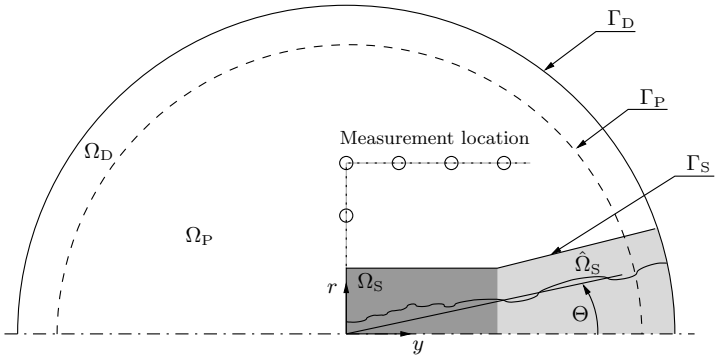

FIGURE 1. Setup for the acoustic computation: volumes Ω_S, Ω_P, Ω_D and corresponding boundary surfaces Γ_S,Γ_P, and Γ_D. The acoustic source-term is confined to Ω_S and the inhomogeneous source region with the variable sound speed is $\Omega_S \cup \hat{\Omega}_S$.

Expanding $p = p_{\text{ref}} + p'$ for small p', and performing the operation $\mathcal{D}_\tau(2.8b) - \nabla_{\boldsymbol{y}}\cdot(2.8a)$, leads to the inhomogeneous wave equation. After neglecting convective terms, which is valid for low Mach number flows (Poinsot & Veynante 2001), the simplified equation can be written as

$$\partial_\tau^2 p' - \nabla_{\boldsymbol{y}} \cdot (a^2 \nabla_{\boldsymbol{y}} p') = \gamma p_{\text{ref}} \left[\text{Da} \partial_\tau \left(\frac{\dot{\omega}_\theta}{c_p \theta} \right) + \partial_\tau^2 \ln(R) + \nabla_{\boldsymbol{y}} \boldsymbol{u} : \nabla_{\boldsymbol{y}} \boldsymbol{u} \right] . \tag{2.9}$$

Note that the frequently employed assumption of a constant value for the ratio of specific heats is used. For the methane/air chemistry used here, this assumption is accurate within 10%. The first term on the RHS of Eq. (2.9) represents an acoustic source-term due to heat release, the second term accounts for effects of temporal variation of the molecular weight of the gas mixture, and the last term is the "shear-refraction term" (Doak 1972). It has been pointed out by Goldstein (1976) and others that this term, rather than being a source-term, is associated with the propagation of sound waves.

2.2.3. *Finite element formulation*

For the FE computation of the acoustic field, the setup schematically shown in Fig. 1 is considered. The domain for the CAA computation is divided into a source region Ω_S in which the acoustic field is generated; into the region Ω_P, in which the acoustic waves propagates; and into the region Ω_D, where artificial damping and absorbing boundary conditions are applied to approximate the free radiation condition. We first transform the partial differential equations (PDEs) – Eq. (2.6) for Lighthill's analogy and Eq. (2.9) for Phillips' equation – into their corresponding weak form. This is done by multiplying the PDEs with an appropriate test function $\omega \in H^1$†, integrating over the whole domain $\Omega = \Omega_S \cup \Omega_P \cup \Omega_D$, and using Green's integral theorem. This results in the weak formulation of Lighthill's analogy

$$\int_\Omega a_{\text{ref}}^{-2} w \partial_\tau^2 p' \mathrm{d}\Omega + \int_\Omega \nabla_{\boldsymbol{y}} w \cdot \nabla_{\boldsymbol{y}} p' \mathrm{d}\Omega - \oint_{\Gamma_D} w \nabla_{\boldsymbol{y}} p' \cdot \boldsymbol{n} \mathrm{d}\Gamma = \mathcal{T} + \mathcal{F} + \mathcal{Q} = \mathcal{T} + \mathcal{R} , \tag{2.10}$$

† H^1 denotes the Sobolev space defined as $H^1 = \{f \in L^2 | \partial_{x_i} f \in L^2\}$ and L^2 is the space of square integrable functions (Adams 1975).

with

$$\mathcal{T} = -\int_{\Omega_S} \nabla_{\boldsymbol{y}} w \cdot \nabla_{\boldsymbol{y}} \cdot (\rho \boldsymbol{u}\boldsymbol{u}) \mathrm{d}\Omega + \oint_{\Gamma_S} w \nabla_{\boldsymbol{y}} \cdot (\rho \boldsymbol{u}\boldsymbol{u}) \cdot \boldsymbol{n} \mathrm{d}\Gamma \,, \tag{2.11a}$$

$$\mathcal{F} = \int_{\Omega_S} \nabla_{\boldsymbol{y}} w \cdot \partial_\tau ((1-\rho)\boldsymbol{u}) \mathrm{d}\Omega - \oint_{\Gamma_S} w \partial_\tau ((1-\rho)\boldsymbol{u}) \cdot \boldsymbol{n} \mathrm{d}\Gamma \,, \tag{2.11b}$$

$$\mathcal{Q} = -\mathrm{Da} \int_{\Omega_S} w \partial_\tau \left(\frac{\dot{\omega}_C}{\rho} \partial_C \rho \right) \mathrm{d}\Omega \,, \tag{2.11c}$$

$$\mathcal{R} = -\int_{\Omega_S} w \partial_\tau^2 \rho \mathrm{d}\Omega \,, \tag{2.11d}$$

and in the weak formulation of Phillips' equation

$$\int_\Omega w \partial_\tau^2 p' \mathrm{d}\Omega + \int_\Omega a^2 \nabla_{\boldsymbol{y}} w \cdot \nabla_{\boldsymbol{y}} p' \mathrm{d}\Omega - \oint_{\Gamma_D} a^2 w \nabla_{\boldsymbol{y}} p' \cdot \boldsymbol{n} \mathrm{d}\Gamma = \mathcal{S} + \mathcal{G} + \mathcal{H} \,, \tag{2.12}$$

with

$$\mathcal{S} = \gamma p_{\mathrm{ref}} \int_{\Omega_S} w \nabla_{\boldsymbol{y}} \boldsymbol{u} : \nabla_{\boldsymbol{y}} \boldsymbol{u} \mathrm{d}\Omega \,, \tag{2.13a}$$

$$\mathcal{G} = \gamma p_{\mathrm{ref}} \int_{\Omega_S} w \partial_\tau^2 \ln(R) \mathrm{d}\Omega \,, \tag{2.13b}$$

$$\mathcal{H} = \gamma p_{\mathrm{ref}} \mathrm{Da} \int_{\Omega_S} w \partial_\tau \left(\frac{\dot{\omega}_\theta}{c_{\mathrm{p}} \theta} \right) \mathrm{d}\Omega \,. \tag{2.13c}$$

On the outer boundary Γ_{D}, absorbing boundary conditions of first order according to Engquist & Majda (1977) are applied by employing the relation

$$\nabla_{\boldsymbol{y}} p' \cdot \boldsymbol{n} = -\frac{1}{a} \partial_\tau p \,. \tag{2.14}$$

Using standard nodal finite elements, we arrive at the following semi-discrete Galerkin formulation (Kaltenbacher 2004)

$$\mathbf{M} \ddot{\boldsymbol{p}}_{n+1} + \mathbf{C} \dot{\boldsymbol{p}}_{n+1} + \mathbf{K} \boldsymbol{p}_{n+1} = \boldsymbol{f}_{n+1} \,, \tag{2.15}$$

with $\ddot{\boldsymbol{p}} = \partial_\tau^2 p'$, $\dot{\boldsymbol{p}} = \partial_\tau p'$, $\boldsymbol{p}$ the nodal unknowns of the acoustic pressure, and n the time step counter. The nodal vector $\boldsymbol{f}_{n+1}$ on the right-hand side is computed according to Eqs. (2.11) for Lighthill's analogy and according to Eq. (2.12) for Phillips' equation. Note that we decreased the computed source-terms within our FE formulation near the boundary Γ_{S} to zero, which means that all surface integrals over Γ_{S} (see Eqs. (2.11)) can be neglected.

The time discretization is performed by applying an implicit Newmark algorithm, which is unconditionally stable and second order accurate (Hughes 1987). The damping matrix $\mathbf{C}$ contains on the one hand the contributions of the boundary integrals over Γ_{D} and on the other hand the artificial damping modeling the sponge layer. The damping is introduced by Rayleigh's damping model (Hughes 1987), where the damping factors appearing in the mass and stiffness matrix have a value of zero at Γ_{P} and increase exponentially toward Γ_{D} within Ω_{D} (see Fig. 1).

TABLE 1. Reference parameters for the reactive jet simulation.

Parameter	Value	Units
D_{ref}	8×10^{-3}	m
U_{ref}	42.2	m/s
ρ_{ref}	1.169	kg/m^2
Re	14,740	-
Sc	0.486	-
Ec	5.4×10^{-5}	-
$\mathrm{M_J}$	0.123	-
Da	0.644	-

3. Numerical simulation

3.1. *Experimental conditions*

The N_2-diluted CH_4-H_2/air flame considered here has been experimentally studied by Bergmann *et al.* (1998), Meier *et al.* (2000), and Schneider *et al.* (2003). The burner configuration for the non-premixed flame consists of a central fuel nozzle of diameter D_{ref} and is surrounded by a co-flow nozzle of square shape. The fuel bulk velocity is U_{ref}. Co-flow air is supplied at an axial velocity of $7.11 \times 10^{-3} U_{\mathrm{ref}}$. All reference quantities used in the calculation are given in Table 1 and Ihme *et al.* (2006). The jet fluid consists of a mixture of 22.1 % methane, 33.2 % hydrogen, and 44.7 % nitrogen by volume with a stoichiometric mixture fraction of $Z_{\mathrm{st}} = 0.167$.

3.2. *Numerical setup for LES*

The Favre-filtered conservation equations for mass, momentum, mixture fraction, and progress variable are solved in a cylindrical coordinate system using a structured LES code. The geometry has been non-dimensionalized with the jet nozzle diameter D_{ref}. The spatial extend of the computational domain in axial and radial direction is 70×30, respectively. For the discretization of the axial direction, 342 grid points are used, which are concentrated near the nozzle and the grid is coarsened with increasing downstream distance from the nozzle. A section of the fuel pipe with a length of three nozzle diameters is included in the computational domain. For the discretization of this section, 40 evenly spaced grid points are used, corresponding to $\Delta y^+ \approx 45$. The radial direction is discretized by 150 unevenly spaced grid points, localized in the region of the shear layer, and 27 grid points are used to discretize the fuel nozzle ($\Delta r^+ \approx 6$ at the wall). The non-dimensional minimum and maximum filter widths in the domain are $\Delta_{\mathrm{min}} = 3.32 \times 10^{-2}$ and $\Delta_{\mathrm{max}} = 1.04$.

A turbulent inlet velocity profile is imposed as inflow condition. This profile is obtained by separately performing a periodic pipe-flow simulation. Convective outflow conditions are used at the outlet and slip-free boundary conditions are employed at radial boundaries.

The chemistry is described using the GRI 2.11 mechanism (Bowman *et al.* 1997) and only stably burning solutions of the steady flamelet equations are used in the flamelet library (Ihme *et al.* 2006).

3.3. *Numerical setup for CAA*

For the spatial discretization of the total computational domain, 5.5×10^6 bilinear hexahedral finite elements have been used. According to the minimal wavelength $\lambda_{\min}$, the discretization parameter h is chosen to be $\lambda_{\min}/20$ in Ω_{S} and Ω_{P} and $\lambda_{\min}/10$ in Ω_{D}. This results in a dispersion error of 0.04% and 0.7%, respectively, under the assumption of non-deformed hexahedral elements (Ainsworth 2004). Furthermore, the time step size $\Delta\tau$ has been set to $1/(25\, f_{\max})$, where $f_{\max}$ denotes the highest frequency of the temporally resolved source-term in the LES.

Since the acoustic field simulation and the LES are performed on different grids, the acoustic source-terms are interpolated onto the acoustic grid. This task is done using a bilinear interpolation, and, to keep the interpolation error small, the grid sizes in the source region of the two grids have been generated such that they do not differ very much. In the present case, the ratio of cells on the LES side to cells on the acoustic side was about 1.9 million to one million. In addition, the acoustic nodal loads are filtered before the acoustic field is computed. The filter characteristic is described in Ihme *et al.* (2006).

4. Results

4.1. *Source-term analysis*

Lighthill's acoustic analogy (Eq. (2.6)) and Phillips' equation (Eq. (2.9)) have different source characteristics. While Lighthill's source-term is composed of Reynolds stress tensor, fluctuating momentum flux vector, and a source-term due to chemical reaction, the RHS in Phillips' equation consists of a heat release term, a source contribution due to local and temporal changes in the molecular weight of the gas mixture, and a "shear-refraction term." The different nature of the source-terms can be attributed to the different model assumptions made during the derivation of the models. Therefore it appears not suitable to directly compare the source behavior between the two models. An analysis of the temporal and spatial evolution of the individual contributions and its relative strength appears to be of greater relevance and interest.

The instantaneous source-term distribution for both Lighthill's analogy and Phillips' equation along a constant r-y plane is shown in Fig. 2. The source-term contributions in Lighthill's analogy are presented in the left column of this figure; the right column shows the three source-term contributions in Phillips' equation. Note that in order to allow for a comparison of the sources, all source-terms in Lighthill's analogy are multiplied by a_{ref}^2. The spatial extend of the magnitude of the source-terms decreases for $y > 15$ and the contributions $\mathcal{T}$, $\mathcal{F}$, and $\mathcal{R}$ are localized in the turbulent shear layer and the transition region after the potential core closes. The chemical source-terms $\mathcal{Q}$ and $\mathcal{H}$ are confined to a region that is very much correlated with the location of stoichiometric conditions.

The spatial distribution of the fluctuating source-term due the variation of the molecular weight of the gas mixture $\mathcal{G}$ indicates the location where the gas composition changes, which is essentially on the rich side of the heat-release region. In the lean region towards the flame, the molecular weight of the mixture is approximately constant, since it is mostly governed by nitrogen. On the rich side, however, the molecular weight changes from that of stoichiometric conditions to that of the fuel, which can be substantially different. This term is consequently mainly confined to rich flame conditions, and its structure is considerably different from that of the "shear-refraction term" $\mathcal{S}$.

The temporal evolution of the different source-term contributions at three locations is

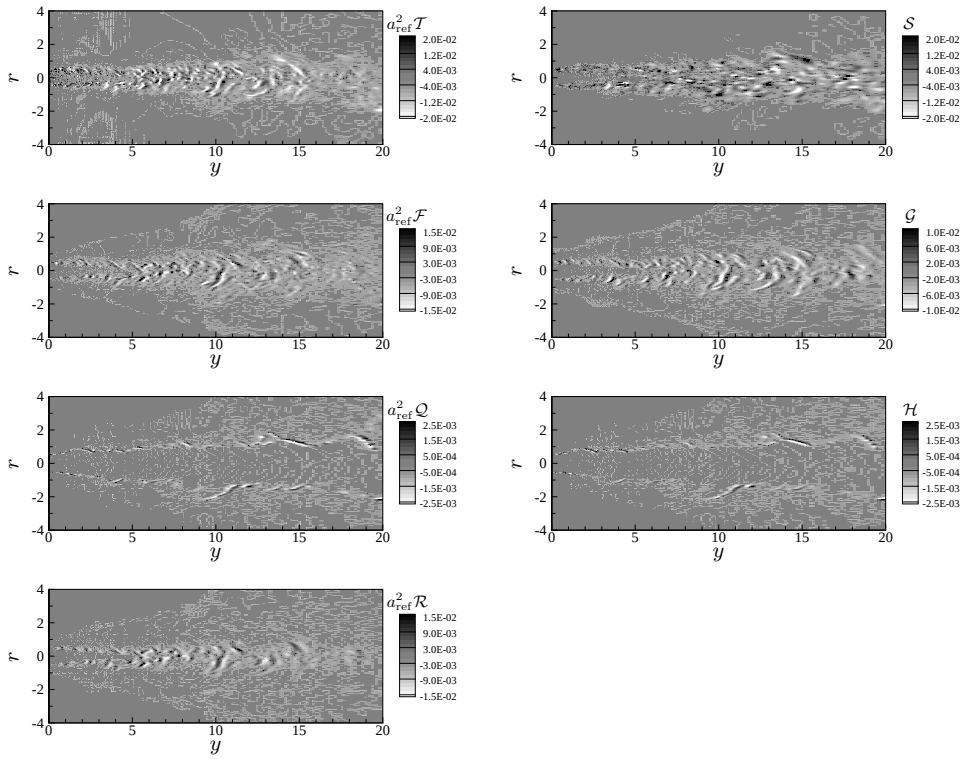

FIGURE 2. Instantaneous source-term distribution. Left column: Lighthill's acoustics analogy, right column: Phillips' equation.

shown in Fig. 3. The source-term contributions in Lighthill's equation are shown in the left column of this figure; the Phillips' source-terms are presented in the right column.

Focusing first on Lighthill's analogy, the magnitude of the chemical source-term (dash-dotted line) is virtually negligible compared to the other source-terms. This appears to be surprising because it has been shown by experimental and theoretical means that this term has the strongest contribution to the far field pressure fluctuations. The reason that this term appears to be small is twofold. First, due to the spreading of the jet, the location of acoustic sources due to chemical reaction is of a conical shape that is not aligned with the measurement points taken along the nozzle lip line. Secondly, the different source-term contributions follow a different radial decay. This can be shown best by the example of a stationary point source of monopole, dipole, and quadrupole type. The constant coefficient wave equation for this case can be written as

$$\partial_\tau^2 p' - a_{\mathrm{ref}}^2 \Delta_{\boldsymbol{y}} p' = \partial_\tau q + \nabla_{\boldsymbol{y}} \cdot \boldsymbol{f} + \nabla_{\boldsymbol{y}} \cdot \nabla_{\boldsymbol{y}} \cdot \underline{t}\,, \tag{4.1}$$

with $q = \breve{q}(\tau)\delta(\boldsymbol{y})$, $\boldsymbol{f} = \breve{\boldsymbol{f}}(\tau)\delta(\boldsymbol{y})$, and $\underline{t} = \breve{\underline{t}}(\tau)\delta(\boldsymbol{y})$. Then the far field pressure for $\boldsymbol{x} \gg \lambda$

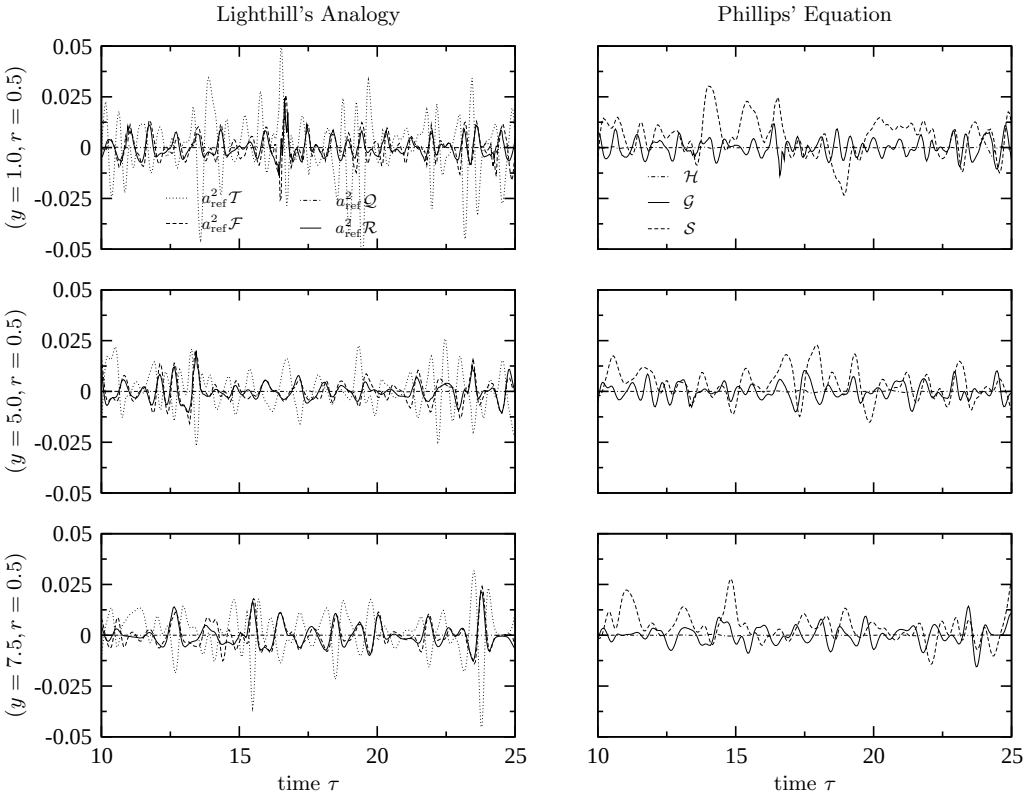

FIGURE 3. Time signal of the acoustic source-terms appearing in Lighthill's analogy and Phillips' equation.

and time t generated by the different sources is

$$\text{Monopole:} \qquad p'_q(\boldsymbol{x},t) \approx \frac{1}{4\pi}\frac{1}{|\boldsymbol{x}|}\frac{\partial \check{q}}{\partial t}\,, \tag{4.2a}$$

$$\text{Dipole:} \qquad p'_f(\boldsymbol{x},t) \approx \frac{1}{4\pi a_{\rm ref}}\frac{x_i}{|\boldsymbol{x}|^2}\frac{\partial \check{f}_i}{\partial t}\,, \tag{4.2b}$$

$$\text{Quadrupole:} \qquad p'_t(\boldsymbol{x},t) \approx \frac{1}{4\pi a_{\rm ref}^2}\frac{x_j x_i}{|\boldsymbol{x}|^3}\frac{\partial^2 \check{t}_{ij}}{\partial t^2}\,. \tag{4.2c}$$

It can be seen from this simplified analysis that the dipole and quadrupole sources are characterized by a directivity and that the source-term strength decreases by a factor $a_{\rm ref}$ between monopole and dipole and dipole and quadrupole, respectively.

4.2. *Effects of variable sound speed*

Heat release by exothermic chemical reaction and heat diffusion out of the reaction zone lead to large changes in temperature across the flame. The temporal changes are accompanied by changes in the local sound speed and alternation of the acoustic field.

Acoustic ray theory can be used when the length scale on which the fluid properties change is large compared to the acoustic wave length. In this case the spatial variations in the sound speed cause refraction of acoustic rays and a change of the wavelength according to $\lambda = a/\mathrm{St}$. Furthermore, the conservation of acoustic energy along the ray

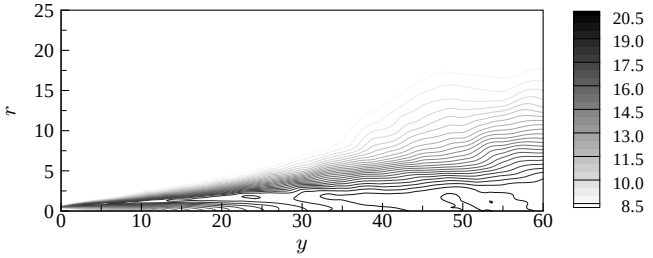

FIGURE 4. Mean sound speed (normalized to U_{ref}) obtained from LES of DLR flame A.

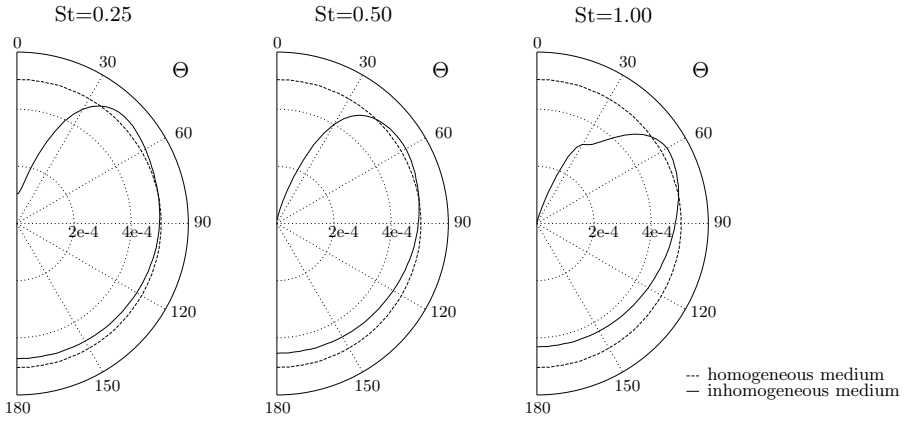

FIGURE 5. Directivity pattern of $|\hat{p}(\mathrm{St})|$ along a circle of radius 50 for point source $100\delta(\boldsymbol{y})\sin(2\pi\mathrm{St}\tau)$ and $\mathrm{St} = \{0.25, 0.50, 1.00\}$.

requires that the amplitude changes according to $p \propto \sqrt{\langle\rho\rangle\langle a\rangle/A(\boldsymbol{y})}$, where A is the cross section of the ray tube (Lighthill 1978).

In this section, the effect of the refraction and attenuation of acoustic waves is studied using a configuration in which a time-harmonic point source is located at the origin and the emitted acoustic wave propagates through an inhomogeneous acoustic medium. For a realistic representation of the medium, the sound-speed field corresponds to the mean field obtained from the LES of the DLR flame. The mean field of the sound speed is shown in Fig. 4. Phillips' equation with spatially varying mean sound speed and RHS defined by $100\delta(\boldsymbol{y})\sin(2\pi\mathrm{St}\tau)$, is solved numerically in an axisymmetric configuration. The pressure signal is recorded along a half circle of radius 50 for different frequencies and is shown in Fig. 5. Note that the angle Θ corresponds to the angle from the downstream jet axis. Three different cases for $\mathrm{St} = 0.25$, 0.50, and 1.0 are considered (solid line) and compared to the solution obtained for a homogeneous medium (dashed line) at ambient conditions. The angle of 30° corresponds hereby approximately to the location of the jet half width. The sound pressure level inside this cone rapidly decreases due to refraction and results in a "zone of silence." The amplitude of the wave traveling in the direction aligned with the centerline decreases with increasing frequency. This implies that waves with higher frequencies exhibit stronger refraction. Caused by the refraction, the monopole source emits acoustic waves in a preferred direction away from the jet axis. This angle increases from 45° to 60° for $\mathrm{St} = 0.25$ to $\mathrm{St} = 1$. Interestingly, it can also be seen that the intensity in backward direction, i.e., for $\Theta > 90°$ reduces also with increasing frequency.

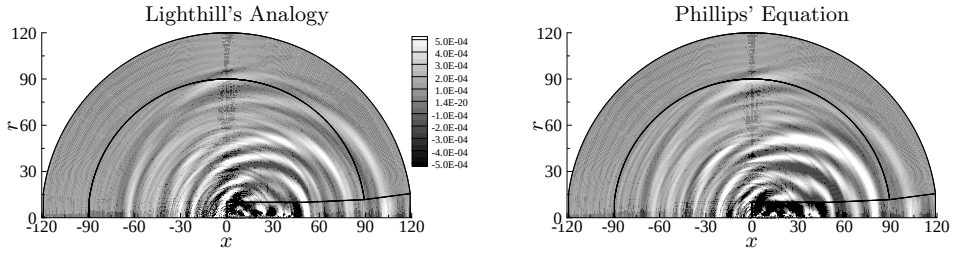

FIGURE 6. Contour plot of instantaneous pressure fluctuation. Left: Lighthill's analogy, right: Phillips' equation without shear refraction term.

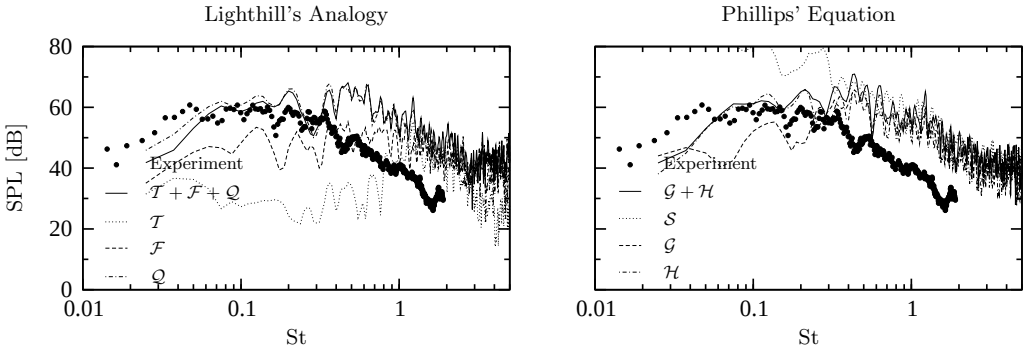

FIGURE 7. Comparison of measured and calculated sound pressure level obtained with Lighthill's analogy (left) and Phillips' equation (right) for constant sound speed.

4.3. *Acoustic results: Lighthill's analogy and Phillips' equation*

Results obtained using Lighthill's analogy and Phillips' equation applied in simulations of the DLR flame are presented and compared with experimental data below.

Figure 6 shows instantaneous pressure distributions, obtained from the hybrid method using Lighthill's analogy (left) and using Phillips' equation without shear refraction term (right). The radiation characteristics obtained from both methods is similar. However, it appears that the pressure field computed using Phillips' equation has a more pronounced radiation in forward direction.

The sound pressure level (SPL) at the measurement location ($x = 0, r = 50$) is compared between experiment and numerical simulation in Fig. 7. The left figure shows the comparison between experiment and simulation for the different source-term contributions in Lighthill's analogy. Results obtained from Phillips' equation are shown in the right figure. Experimental data are denoted by symbols.

Focusing first on results obtained from Lighthill's analogy, it can be noted that the numerical results in the low frequency range, i.e., for $\mathrm{St} < 0.3$ (corresponding to ~ 1600 Hz) are in good agreement with experimental data. The sound pressure level for frequencies above $\mathrm{St} = 0.3$ is over-predicted. The reason for this discrepancy is under investigation. The individual source-term contributions to the sound pressure level are also presented in the same figure. The contribution from the Reynolds stresses is negligible. In the low frequency range, the chemical source-term represents the most important acoustic source. These findings are in agreement with results presented in Ihme *et al.* (2006).

Phillips' equation with constant sound speed and exclusion of the shear refraction term leads to similar results, obtaining good agreement in the low frequency range. The

sound pressure level obtained from including the shear refraction term is over-predicted; the reason for this is under investigation. Apart from this discrepancy it is shown that the source-term accounting for the variation of the gas constant of the mixture is small compared to the heat release term. Overall, the agreement of the SPL in the low frequency range is in reasonable agreement between experiment and simulation.

5. Conclusions and further work

A hybrid LES/CAA method for the prediction of combustion-generated noise has been developed. The acoustic field is solved using an FE code and the acoustic source-terms obtained from a low Mach number variable-density LES solver are interpolated onto the acoustic grid. For the treatment of the open boundaries in the acoustic domain, absorbing boundary conditions and a sponge layer technique are employed. Two acoustic analogies, Lighthill's analogy and Phillips' equation, were employed. The latter analogy accounts for refraction effects due to variable sound speed, caused by the heat release.

The hybrid approach was applied in numerical simulations of an N_2-diluted CH_4-H_2/air flame. The individual acoustic source-terms, appearing in both analogies, were analyzed, and the effect of the inhomogeneous medium on the directivity pattern was investigated. Results for the sound pressure level are compared with experimental data. Reasonable agreement between experiments and simulation is obtained for the low frequency range, i.e., for $\mathrm{St} < 0.3$. The sound pressure level at higher frequencies is over-predicted. This discrepancy requires additional investigation.

Further work includes the analysis of the "shear-refraction term" appearing in Phillips' equation, directivity patterns of the different source-terms, and the quantification of the grid sensitivity of the LES on the acoustic pressure.

Acknowledgments

The authors gratefully acknowledge helpful discussions with Thierry Poinsot, Franck Nicoud, and Sanjiva Lele.

REFERENCES

Adams, R. 1975 *Sobolev Spaces*. Academic Press.

Ainsworth, M. 2004 Discrete Dispersion Relation for hp-Version Finite Element Approximation at High Wave Number. *SIAM J. Numer. Anal.* **42** (2), 553–575.

Balsa, T. 1976 Refraction and shielding of sound from a source in a jet. *J. Fluid Mech.* **76** (3), 443–456.

Bergmann, V., Meier, W., Wolff, D. & Stricker, W. 1998 Application of spontaneous Raman and Rayleigh scattering and 2D LIF for the characterization of a turbulent $CH_4/H_2/N_2$ jet diffusion flame. *Appl. Phys. B* **66** (4), 489–502.

Bowman, C., Hanson, R., Davidson, D., Gardiner, W., Lissianski, V., Smith, G., Golden, D., Frenklach, M. & Goldenberg, M. 1997 GRI-Mech 2.11. Available from http://www.me.berkeley.edu/gri-mech/.

Doak, P. 1972 Analysis of internally generated sound in continuous materials: 2. critical review of conceptual adequacy and physical scope of existing theories of aerodynamic noise, with special reference to supersonic jet noise. *J. Sound Vib.* **25** (2), 263–335.

Durbin, P. 1983*a* High frequency Green function for aerodynamic noise in moving media, Part I: General theory. *J. Sound Vib.* **91** (4), 519–525.

Durbin, P. 1983*b* High frequency Green function for aerodynamic noise in moving media, Part II: Noise from a spreading jet. *J. Sound Vib.* **91** (4), 527–538.

Engquist, B. & Majda, A. 1977 Absorbing Boundary Conditions for the Numerical Simulation of Waves. *Mathematics of Computation* **31**, 629–651.

Ffowcs Williams, J. 1977 Aeroacoustics. *Ann. Rev. Fluid Mech.* **9**, 447–468.

Goldstein, M. E. 1976 *Aeroacoustics*. New York: McGraw-Hill.

Hughes, T. 1987 *The Finite Element Method*, 1st edn. New Jersey: Prentice-Hall.

Ihme, M., Bodony, D. & Pitsch, H. 2006 Prediction of combustion-generated noise in non-premixed turbulent jet flames using large-eddy simulation. *AIAA Paper 2614*.

Kaltenbacher, M. 2004 *Numerical Simulation of Mechatronic Sensors and Actuators*. Springer Berlin-Heidelberg-New York.

Kotake, S. 1975 On combustion noise related to chemical reactions. *J. Sound Vib.* **42** (3), 399–410.

Lighthill, M. J. 1952 On sound generated aerodynamically: I: General theory. *Proc. Roy. Soc. London (A)* **211** (1107), 564–587.

Lighthill, M. J. 1978 *Waves in Fluids*. Cambridge University Press.

Lush, P. 1971 Measurements of subsonic jet noise and comparison with theory. *J. Fluid Mech.* **46** (3), 477–500.

Meier, W., Barlow, R., Chen, Y. & Chen, J. 2000 Raman/Rayleigh/LIF measurements in a turbulent $CH_4/H_2/N_2$ jet diffusion flame: Experimental techniques and turbulence-chemistry interaction. *Combust. Flame* **123** (3), 326–343.

Pao, S. 1973 Aerodynamic noise emission from turbulent shear layers. *J. Fluid Mech.* **59** (3), 451–479.

Phillips, O. M. 1960 On the generation of sound by supersonic turbulent shear layers. *J. Fluid Mech.* **9** (1), 1–28.

Pierce, C. & Moin, P. 2004 Progress-variable approach for large-eddy simulation of non-premixed turbulent combustion. *J. Fluid Mech.* **504**, 73–97.

Poinsot, T. & Veynante, D. 2001 *Theoretical and Numerical Combustion*. Philadelphia, PA: R.T. Edwards, Inc.

Schneider, C., Dreizler, A., Janicka, J. & Hassel, E. 2003 Flow field measurements of stable and locally extinguishing hydrocarbon-fuelled jet flames. *Combust. Flame* **135** (1-2), 185–190.

Singh, K. K., Frankel, S. H. & Gore, J. P. 2003 Effects of combustion on the sound pressure generated by circular jet flows. *AIAA J.* **41** (2), 319–321.

Singh, K. K., Frankel, S. H. & Gore, J. P. 2004 Study of spectral noise emissions from standard turbulent nonpremixed flames. *AIAA J.* **42** (5), 931–936.